# Effects of as-built surface with varying number of contour passes on high-cycle fatigue behavior of additively manufactured nickel alloy 718

Orion L. Kafka[a,*], Jake Benzing[a], Nicholas Derimow[a], Philipp Schumacher[b], Lucas Koepke[d], Chad Beamer[c], Donald Godfrey[b], Nikolas Hrabe[a,*]

[a] *Applied Chemicals and Materials Division, Material Measurement Laboratory, National Institute of Standards and Technology, Boulder, CO 80305, USA*
[b] *SLM Solutions, 48561 Alpha Drive, Suite 300, Wixom, MI 48393, USA*
[c] *Quintus Technologies, 8270 Green Meadows Drive North, Lewis Center, OH 43035, USA*
[d] *Statistical Engineering Division, Information Technology Laboratory, National Institute of Standards and Technology, Boulder, CO 80305, USA*

## Abstract

High cycle fatigue life of laser-powder bed fusion (L-PBF) parts depends on several factors; as-built surfaces, when present, are a particular concern. This work measures as-built L-PBF surfaces with X-ray computed tomography, and uses rotating beam fatigue testing to measure high cycle fatigue life. Surfaces with different, but consistent, characteristics are achieved by building vertical specimens and changing only the number of contour passes. In this way, specimens with three different levels of surface roughness are compared to standard polished specimens. The results from this show that surface roughness increases with decreasing number of contour passes, but the impact on fatigue lifetime is not trivially related. Electron microscopy and x-ray computed tomography images show multiple initiation points and complex surface topology, but that surface feature depth is not necessarily correlated to failure location. Two primary conclusions are that 1) for the case of as-built surfaces loaded in bending, one contour pass is sufficient to achieve peak as-built performance; 2) surface feature depth, even when measured using metal-penetrating imaging, is not strongly associated with failure location in our data. When assessing AM surfaces, more factors (e.g., grain orientation) may be required to mechanistically understand the performance implications.

*Keywords:* Additive manufacturing, Laser powder bed fusion, Rotating beam fatigue, Nickel alloy 718, As-built, surface roughness

## 1. Introduction

Laser powder bed fusion (L-PBF) is perhaps the most prevalent metal additive manufacturing (AM) technology currently in use. However, concerns over the fatigue

*Corresponding authors: orion.kafka@nist.gov, nik.hrabe@nist.gov

life of materials produced with L-PBF still limit the widespread use of the material in critical components. Progress has been made in recent years, but open questions remain. One reason for concern is the poor finish of as-built surfaces relative to machined parts. Such surfaces can lead to both increased fatigue life variability and an overall fatigue life (or strength) deficit. Many different techniques exist to modify as-built surfaces, e.g., line-of-sight (shot peening, machining) and non-line-of-sight (electro-chemical abrasion, hydrodynamic cavitation erosion) [1]. However, in some cases it is necessary to skip such post-processing due to cost, time, access, or other constraints.

One common technique that AM system manufacturers use to reduce surface roughness in the as-produced condition is *contour passes* (or sometimes called *borders*), where the outline of the part is traced by the laser either before or after the interior of the part is scanned. For example two contour passes might be used, potentially with different scan speeds, laser powers, and offsets from the interior in an attempt to produce as smooth a surface as possible. This adds unwanted build time, while also increasing the already-complex parameter space, but can produce smoother surfaces.

Although the impact of volumetric defects such as pores in L-PBF metals been relatively thoroughly studied in recent years, as-built surfaces have not been as widely investigated and thus require further attention. Work from the surface metrology community tells us that as-built surfaces introduce surface roughness [2, 3]. However, the connection of as-built surfaces to fatigue performance has not been widely considered. Although several authors have investigated the impacts of as-built surfaces on fatigue life, they have mostly focused on surface modification rather than the fundamentals of as-built surface mechanics. Studies of surface post-treatment have been reviewed by Maleki *et al.* [1]. Relevant studies related to fatigue in AM IN718 specifically have been summarized by the recent work of Sadeghi *et al.* [4]. Only a few of these studies have investigated the impact of as-built surfaces on fatigue performance of L-PBF IN718. This relative dearth of cited works in such an extensive review suggests that more work is needed to understand the mechanics and corroborate existing evidence.

For as-built AM nickel alloy 718 (IN718), the following represent the bulk of published studies of fatigue performance to date. Most relevant to the current work, Gockel *et al.* [5] studied the impact of changing contour processing parameters on surface roughness and fatigue life, although some of the contour parameter settings may have resulted in only partial attachment of the outer skin, making interpretation difficult. Witkin *et al.* [6], Konečná and Nicolleto [7], and Nicoletto [8] studied the impact that build orientation has on fatigue performance with as-built surfaces, including for notched geometry specimens. However, this introduces uncontrolled variables due to upskins and downskins. Upskins are angled or top surfaces where the melt pool to is fully or partially exposed to unmelted powder in the build chamber, and downskins and the opposite, where overhangs result in the bottom of the melt pool being exposed to unmelted powder. Either condition significantly change the surface morphology expressed by the as-built part. This makes the results hard to decipher. Solberg *et al.* [9] also studied notch effects, including micro-notches resulting from layer-stacking. Balachandramurthi *et al.* [10] chose to quantify as-built surfaces using a top-down focus-variation microscope and only reports summary statistics ($S_z$, $S_v$, and $S_a$). Due to the complex topology of AM surfaces, it is possible that these statistics fail to accurately capture the surface and near-surface features, which are of primary importance in fatigue, an issue that has been ably described by Lee *et al.* [11].

One difficulty with testing as-built surfaces is that they do not conform to standardized materials testing protocols (e.g., ASTM E466/E606 [12] specifies testing polished specimens by default), which necessarily adds complexity to the study design. However, if the AM process is to be optimized for material performance, the impact of factors such as contour passes must be fully understood in order to optimize the process. This will enable the use parts where surface treatments are impractical or impossible to achieve, for example, parts with fully enclosed interior cavities.

Another challenge with the existing literature is that most authors use manufacturer-supplied default settings and only report the few build parameters they have worked with directly. Additionally, alloy composition, when given, is often simply the material specification rather than the true composition of the feedstock and resulting built material. To make fair comparisons possible, it is important to adhere to the relevant reporting standards, such as those of the ASTM Standards organization [13], when reporting results and publishing in open literature. These issues are brought up by Sadeghi *et al.* [4], but are worth reiteration because of the challenge it imparts when attempting to find equivalent studies, reproduce results, or simply use the results of published papers. Herein we attempt to provide as many details as possible to describe the build conditions, feedstock, processing, and specimens to avoid this common pitfall currently plaguing many papers and reports in the metal AM community.

The collection of work discussed above indicates that as-built surfaces are detrimental to fatigue life, due to the mechanism of surface notches acting as stress-raisers. Due to the challenges mentioned, it is difficult to comprehensively understand the relationship between AM build parameters, surface roughness, and fatigue performance because of factors such as: under-reported build conditions, uncontrolled variables, ambiguous or under-specified alloy composition, small and/or unpublished raw data sets, and the aforementioned difficulties associated with using traditional surface metrology techniques developed for relatively smooth machined parts on the complex topography of as-built AM surfaces.

To address this limitation in the literature, the current work studies the impact of as-built surfaces on fatigue life. The study was designed to, insofar as possible, include only one variable—the surface condition as controlled by number contour passes. This was isolated by our study design (see the Methods section 2 for details). The study tests if 0-, 1-, and 2-contour passes changes the 3D topology of the surfaces, and if fatigue performances is related to these changes (see the Results section 3). To state this as a question, we ask: how much of a fatigue performance deficit does using two, one, or zero (hatch-only) contour passes impose compared to a polished surface under high cycle ($1 \times 10^5$ cycles to $1 \times 10^7$ cycles) fatigue loading conditions? One consequence of this research is that if fatigue properties of 1- or 0-contour conditions are similar to the 2-contour performance, or fit-for-purpose in an design application, one could achieve process speed-up by using the minimum number of contour passes necessary.

## 2. Materials and Methods

### *2.1. Additive manufacturing material and process*

Specimens were built using nickel-based superalloy IN718 using an SLM 280 Production Series dual laser machine[1]. All specimens were built with virgin, single-lot powder that was Argon gas atomized and sieved such that 99% of particles failed to pass a 45 µm sieve while no particles failed to pass a 53 µm sieve . This resulted in a measured size range described by $D_V(10) = 18$ µm, $D_V(90) = 50$ µm, and $D_V(50) = 30$ µm, where $D_V(x) = y$ describes the diameter ($y$) below which contains $x$ volume fraction of material. In other words, 90% by volume of powder is contained within particles that are ≤50 µm in diameter, as measured by laser diffraction (ASTM B822). Pre-build powder chemistry and post-build solid chemistry were measured (Table 1) to be within specification for IN718 [14] and are similar to each other (i.e., Al, Cr, Mo, Nb+Ta, Ni, Si, and Ti are enriched between 0.04 wt-% and 0.55 wt-%, while the other measured elements are depleted in commensurate proportion). Solid chemistry measurements were conducted at an International Standards Organization (ISO) 17025:2017 compliant and Nadcap accredited test labs using Combustion-Infrared Absorption for Carbon and Sulfur (LECO CS600 and CS844), Thermal conductivity Nitrogen and Infrared Oxygen and Hydrogen Analyzer (LECO ONH836, for N, O, and H), and Inductively Coupled Plasma Atomic Emission Spectroscopy for the remaining elements.

The parameters used for this build are summarized in Table 2. Automated powder supply and permanent filtering modules were fitted to the SLM 280. Block support and additional pins were used to protect the specimens during the build. Preliminary work using the same parameters on a specifically designed build plate verified that overall dimension, orientation in the build chamber (e.g., if the part faces towards or away from the gas flow inlet), and location on the build plate could be discounted as potential variables. Dimensional fidelity with varying number of contour passes was also checked, to ensure consistent specimen diameter. Finally, surface roughness with different number of contour passes was measured to make sure this would be the dominant factor in full builds. The preliminary build and measurements described in detail in Appendix A.

### *2.2. AM build layout and printed geometries*

Vertically oriented specimens of two different geometries were made following a designed grouping strategy to allow for possible impacts of build plate location on performance. For convenience, we define a coordinate system where Z is the build

[1]Certain commercial equipment, instruments, or materials are identified in this paper in order to specify the experimental procedure adequately. Such identification is not intended to imply recommendation or endorsement by NIST, nor is it intended to imply that the materials or equipment identified are necessarily the best available for the purpose.

Table 1: Nominal [14], pre-build, and post-build chemistry (in wt-%) for the powder and as-built IN718 material. B, Cu and H were not measured (or below reportable limits) in the post-build assay.

| Element | Al | B | C | Co | Cr | Cu |
|---|---|---|---|---|---|---|
| Nominal | 0.20-0.80 | 0.006 Max | 0.08 Max | 1.0 Max | 17.0-21.0 | 0.30 Max |
| Pre-build | 0.53 | <0.0001 | 0.03 | 0.1 | 18.76 | 0.02 |
| Post-build | 0.57 | — | 0.030 | 0.080 | 18.84 | — |

| Element | Fe | H | Mn | Mo | N | Nb(+Ta) |
|---|---|---|---|---|---|---|
| Nominal | Bal | — | 0.35 Max | 2.80-3.30 | — | 4.75-5.5 |
| Pre-build | Bal | <0.01 | 0.03 | 3.07 | 0.01 | 5.01 |
| Post-build | 18.14 | — | 0.028 | 3.22 | 0.008 | 5.354 |

| Element | Ni | O | P | S | Si | Ti |
|---|---|---|---|---|---|---|
| Nominal | 50.0-55.0 | — | 0.015 Max | 0.015 Max | 0.35 Max | 0.65-1.15 |
| Pre-build | 52.04 | 0.02 | 0.004 | 0.001 | 0.04 | 1.00 |
| Post-build | 52.591 | 0.018 | 0.002 | 0.001 | 0.055 | 1.10 |

Table 2: Machine parameters used for the build, using the manufacturer's terminology.

| Build Parameter | Value |
|---|---|
| Scan order | Hatch-Border |
| Build plate preheat temperature | 200 °C |
| Layer height | 30 µm |
| Beam focused spot size | 75 µm |
| Focus | 0 mm |
| Fill pattern type | Stripes |
| Stripe length | 7 mm |
| Rotation angle increment | 67° |
| Rotation limitation window | 135° |
| Hatch distance | 0.09 mm |
| Laser power | 200 W |
| Scan speed | 1200 mm/s |
| Hatch offset (hatch to inner border) | 0 mm |
| Border distance (for 2-border strategy) | 0.08 mm |
| Border order (for 2-border strategy) | Inside-out |
| Border laser power | 150 W |
| Border scan speed | 450 mm/s |

direction, X is towards the gas inlet (against the flow) and Y is along the recoater direction. The build layout is shown in Figure 1. Note that vertical specimens do not have upskin or downskin regions in the gauge section. Specimens were built with one of two lasers (700 W IPG fiber lasers); although specimens were built in the overlap region using both lasers, they are not included in this study to avoid a potential confounding variable. Specimens were embossed with a unique numeric label, traceable to their exact location in the build plate. Additional witness coupons (rectangles for surface and metallurgical shape tests, and larger lighter circles for tensile testing) and powder containers (larger darker cylinders) were also included for build validation.

The build layout was arranged in a grid-in-grid manner, with groups of four test specimens patterned into 25 different sub-regions (leading number in specimen ID) on the build plate. Each group of four specimens contains one specimen from each of the four different conditions studied (trailing number in the specimen ID). For example specimen 20.3 is located on the fourth row up, in the fifth column and is in process condition 3. All specimens used the SLM Solutions standard build template, with the following variations. Specimens marked with a trailing 1 were built using the manufacturers default contouring, which consists of two contour passes. Specimens marked with a trailing 2 were modified to have only one contour pass. Specimens marked with a trailing 3 were modified to have no contour passes (hatching exposed). The build parameters for the infill and contour are given in Table 2. Finally, specimens marked with a trailing 4 were built as cylinders, then machined and polished to provide a baseline of pristine material without surface effects. The machining and polishing process followed ISO 1143:2010(E) and ASTM E466-15 recommended steps [15, 12], see Appendix B.

The as-built surface (0-, 1-, and 2-contour) specimens were designed to be tested using rotating beam fatigue (RBF), and their geometry is shown in Figure 2a). Note that the grip sections of the specimens with as-built surface were slightly over-built and then centerless ground to 12.7 mm diameter to provide a smooth surface to clamp in collets for testing. The designed dimensions of the net-shape (Figure 2a) and polished surface (Figure 2c) specimens are similar. The only difference is that the polished specimens have their a fillet radius increased to 20 mm from 10.15 mm to facilitate polishing, which decreases the grip length slightly. The specimen geometry mostly conforms with the ISO 1143 *Rotating bar bending fatigue testing* recommendations [15] using the constant-cross section geometry to maintain a constant bending stress throughout the full gauge section while under 4-point bending load. However, the radii of the fillets are slightly smaller than recommended. This radius and stair-stepping from the layer-by-layer nature of the build causes stress concentrations at the fillets, although failures in the fillets were uncommon.

### *2.3. As-built tensile properties*

To ensure builds were printed without excessive defects and conformed to the manufacturer's expectations, 10 as-built witness coupons for tension testing were co-located

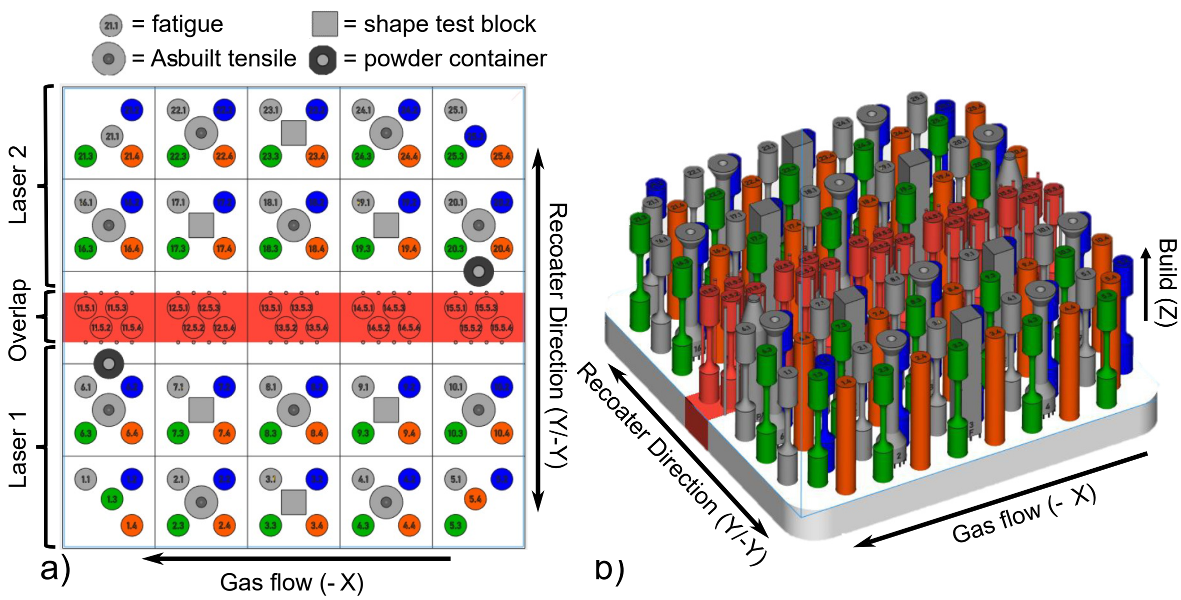


Figure 1: Build layout for fatigue specimens: a) top-down view, b) isometric (3D) rendering. Vertically oriented specimens are built in a grid-in-grid pattern and embossed with labels to avoid location-in-build effects and maintain complete tractability. Colors represent different test conditions: gray = 2 contour passes, blue = 1 contour pass, green = 0 contour passes, and orange = cylinder to be machined and polished. Rectangles are used to test shape and perform metallographic studies (such as chemistry). Larger circles represent specimens used for as-built tensile testing to ensure build quality, and larger dark circles represent powder containers used to capture powder during the build (not currently used). Two lasers were used, and traceability is maintained between the two. Though specimens were made in the overlap region, highlighted in orange, they were not included in the present work to avoid introducing another potential variable.

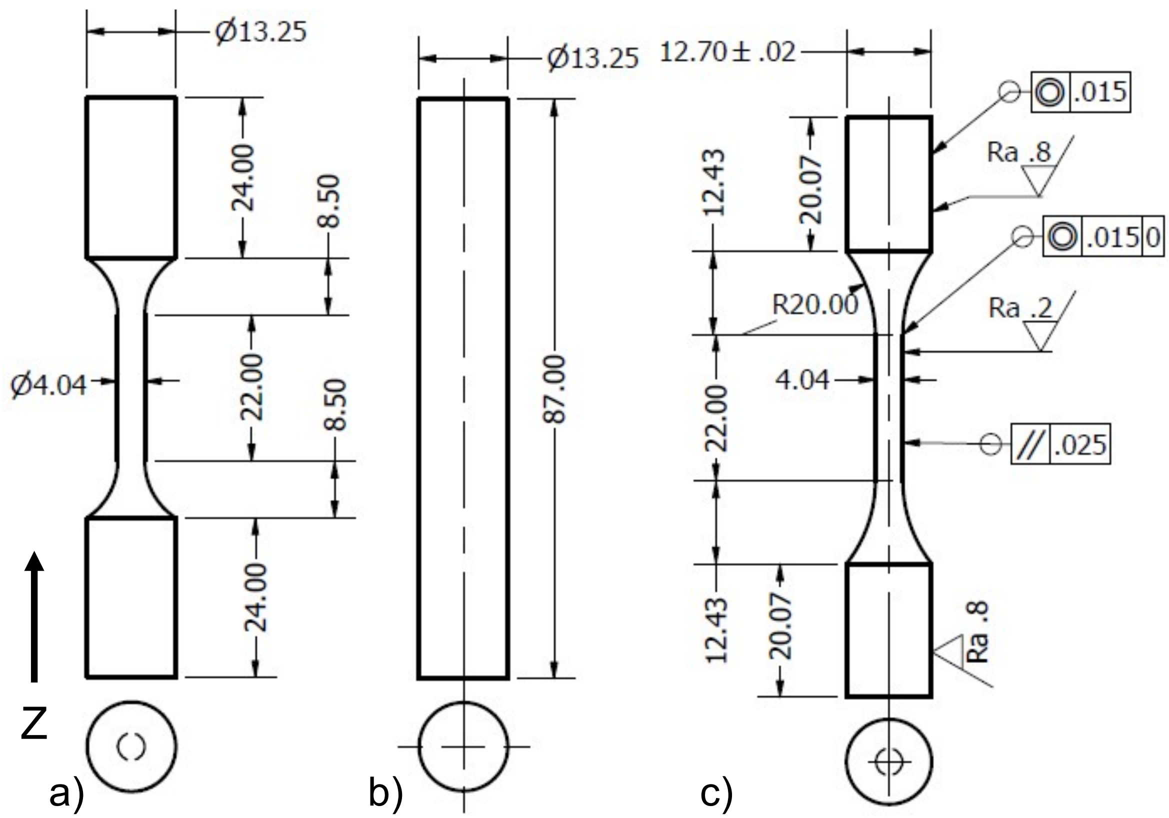


Figure 2: a) as-built specimen geometry for 4-point rotating beam fatigue tests, note that 13.25 mm grips were ground to 12.7 mm for clamping in collets; b) as-built cylinders to be machined into c) fully polished specimens. All dimensions are in millimeters, roughness callouts are micrometers, and tolerances are 0.02 mm unless otherwise noted.

Table 3: Heat treatment steps in the order they were conducted, including a hot isostatic pressing (HIP) step to reduce porosity. Note that the vacuum furnace had a partial pressure of 20 Pa of nitrogen gas.

| Step | Parameters |
|---|---|
| 1. Stress relief | 1.5 h at 1065 °C in vacuum, air cool (AC) to room temp (RT) |
| 2. Hot isostatic pressing | 1150 °C for 4 h at 100 MPa in Ar, furnace cool (FC) to RT |
| 3. Solution | 1066 °C for 1 h, quench to 95 °C, AC to RT |
| 4. Two-step age | 718 °C for 8 h, FC to 621 °C, hold for 10 h, FC to RT |

amongst the fatigue specimens (see Figure 1) Nominal tensile properties were measured from these using standardized testing procedures at a Nadcap certified laboratory.

### *2.4. Heat treatment and grain measurements*

Specimens were cut off the build plates using electrical discharge machining, prior to any post-processing steps. Heat treatment was conducted on the specimens after grip machining for the as-built surface specimens, and before machining for the polished specimens. A IN718 heat treatment commonly used in industry currently following ASM2774 (S1750DP/S1950DP) [16] and ASTM F3055 [14] guidelines, was conducted. This heat treatment consists of the steps outlined in Table 3.

Parts for metallographic examination were excised, ground, and polished using common metallurgical preparation procedures. Electron backscatter diffraction (EBSD) measurements were performed at a step size of 0.5 µm using a field emission scanning electron microscope operated with a 25 kV accelerating voltage and a 19 mm working distance.

### *2.5. Fatigue testing procedure*

Four-point rotating beam fatigue was used to test each specimen, using an ADMET eXpert 9300—Rotating Beam Fatigue machine. Prior to testing, the diameter of each specimen was carefully measured to within ±0.5 µm along the gauge section, with three repeat measures around the circumference for each location (top, middle, bottom). The mean diameter was used compute the bending force necessary to achieve the desired stress level for each test. Across all conditions and all specimens the overall standard deviation in diameter is 0.027 mm, $n = 210$ where $n$ is the number of samples. This is a contact-type measurement and thus does not necessarily represent the exact stresses of the rough surface specimens. However, this does provide a consistent measure with which to compare between specimens measured and tested using the same protocol.

Tests were generally conducted at 30 MPa increments in stress and executed until either failure, or at least $10^7$ cycles. At each increment in stress, a set of specimens from the same sub-region on the build plate were all tested, to minimize possible within-stress-level build variability.

Specimens were mounted by their grip sections into the collets of the RBF machine. This RBF machine uses a linear actuator and load cell calibrated to a working range of

0 N to 220 N to provide feed-back force control, which enables consistently controlled loading and information as to the fluctuation of load during the test. Before the test was started, specimens were loaded to 20 N and manually rotated to measure an estimated *force variability*, i.e. any slight warping (or loss of coaxiality) of the specimen will result in higher forces when in one orientation than when rotated 180°. Specimens with the as-built surface condition tended to have some minor warping, perhaps due to stress relief during heat treatment, which was quantified in this way prior to testing.

Tests were conducted at 6000 RPM, or 100 Hz if one tracks the cyclic stress at one point. The nature of rotating bending testing implies the testing is fully reversed, i.e., stress ratio ($R$) of $R = -1$. However, slight warping in the specimens results in non-symmetric loading, which will be shown as error bars in the results to come. Preliminary tests indicate no adiabatic heating at this frequency for IN718. The tests were conducted in lab air with constant airflow over them during testing. Specimens were measured to reach a steady state of around 28 °C to 32 °C during testing due to their proximity to the hot motor. This temperature fluctuation is unlikely to alter mechanical properties of IN718.

During testing, the force readback signal was collected at a sufficient polling rate to provide information regarding the force variability through the test. Note that due to dramatically different duration of tests and a fixed buffer size available for recording data, the data collection rate changed between specimens. From this, the spread between minimum and maximum force during testing was extracted and is reported along with the mean bending stress to quantify these fluctuations. Ideally the fluctuations would be zero, however, these specimens deviate from ideal conditions due to their as-built nature; the magnitude of the deviations are reported as error bars in the stress-life plot (Figure 8). This force fluctuation is cyclic, likely caused by loss of coaxiality from warping during heat treatment and does not drift with time. The polished condition specimens have negligible fluctuations due to geometry, with all the variability due to force control, which was <2 % of the maximum applied stress.

Tests stopped when one of two conditions were satisfied: a load-drop of 50 % or $1 \times 10^7$ cycles (or more) was reached. The latter condition is termed *runout* and indicated as such on the stress-life plots. Some specimens were run to substantially more cycles, with the most being specimen 6.2, which lasted 304 730 636 cycles (i.e., $3.05 \times 10^8$ cycles) before being stopped. These specimens are shown with truncated lives (to about $1 \times 10^7$ cycles) in the stress-life diagram to enable clearer plotting. The full data are provided in [17]. All specimens were saved, and separated specimens were initial imaged with optical microscopy, and selected specimens were imaged in more detail using electron microscopy. After testing, non-fractured specimens were not retested at a higher stress.

### *2.6. Pre- and post-failure specimen quantification*

Prior to testing, a subset of the as-built surface specimens (specifically, 1.1, 1.2, 1.3, 21.1, 21.2, 21.3) were imaged using micro X-ray Computed Tomography (X-ray CT) to measure the full 3-dimensional (3D) geometry of specimens including internal pores and the rough surfaces. The X-ray CT measurements were conducted on a Zeiss Xradia Versa XRM-500 system. The full specimen gauge sections, and in some cases some amount of the fillets on either end, were scanned using between 4 and 7 fields of view via vertical stitching and 1301 to 1601 projection images collected over 192° for each field of view to achieve a cubic voxel edge length of $(4.50 \pm 0.13)$ µm, where the uncertainty is computed from a calibration artifact-based pixel-size determination. An acceleration voltage of 160 kV and power of 10 W was used with 8 s to 10 s exposure time to achieve satisfactory transmittance, flux density (photons per second per area), and finally counts at the detector. Projections were reconstructed into 3D volume images roughly 983 pixels by 1002 pixels by 6000 pixels using proprietary software included with the instrument. Reconstruction included a beam-hardening correction step, using a beam hardening constant of 0.2 in the proprietary algorithm. After reconstruction, 16-bit grayscale images were exported as multipage TIFF images, and these images were analyzed using open-source Python codes [18].

Image analysis consisted of post-reconstruction local smoothing using the nonlocal means denoising algorithm provided by SciKit-Image [19] to minimize grayscale noise, segmentation using a global Otsu algorithm, and custom analysis of the processed binary images to compute surface feature depth and other parameters of interest. Visualizations were conducted using STL surface meshes computed from the 3D volumetric image using the marching cubes algorithm.

Surface features were numerically described by the distance between the centroid of the specimen and the first metal/air interface found by ray-casting from the centroid towards the edge. Specifically, the distance at which a black pixel was first entered, in this case enforced to be within 450 µm of expected radius (2.02 mm) to avoid possible internal pores, was recorded as the edge of the specimen for that ray. Although this is a non-traditional measurement of the surface, it has the advantage of identifying the absolute minimum radius of material, which is an important factor when considering localized stresses within the material. These radial distances were computed across all angles in each slice, forming a 360° map of the centroid-edge distance, and for all slices from the bottom of the gauge section to the top. In order to identify the deepest surface feature in each slice, the smallest such radius from each slice was extracted as a function of height in the build direction (i.e., slice number). Similarly, a mean distance and maximum distance can be extracted for each slice. Mathematically, the valley depth, as computed from these measurements, is summarized by

$$S_{v,i}^{XCT} = |\mathrm{mean}(r_i(\theta)) - \min(r_i(\theta))|, \tag{1}$$

where $r_i$ is the radius of slice $i$ as a function of angular increment $\theta$, shown schematically in Figure 7b) in the dashed blue line. $S_{v,i}^{XCT}$ can then be plotted as a function of $i$, the height in the build direction, or Z-direction in Figure 1. This differs somewhat from the conventional surface metrology definition of $S_v$ of surface-derived valley depth, and thus is not directly comparable with $S_v$. One benefit of this technique is that it provides an indicator of the depth of surface features regardless of overhanging material, and thus

Table 4: Maximum, minimum, and mean tensile properties of as-built witness coupons co-located on the build plate with the fatigue coupons ($n = 10$). This shows relatively low scatter and nominal (expected) performance for the as-built conditions, confirming that the build was successful.

| | Min. | Mean | Max. |
|---|---|---|---|
| 0.2% Yield | 678 MPa | 685 MPa | 697 MPa |
| Ultimate tensile strength | 973 MPa | 979 MPa | 986 MPa |
| Total elongation | 30.5 % | 31.4 % | 32.6 % |

may provide a stronger correlation to peak stress zones are subjected to loading. For these specimens, we specifically use the radius from the centroid. This is because in the bending configuration, stress will depend upon the distance from the zero-stress axis. Note that for axial fatigue, a measurement such as minimum total diameter would be computed instead.

### *2.7. Fractography*

Scanning electron microscopy (SEM) was performed at an accelerating voltage of 5 kV to investigate the fracture surfaces, both over large areas and at high resolution over smaller regions of interest (ROIs). Screening was conducted using optical microscopy and low resolution SEM to select specimens of interest with clearly visible, representative failure features. For rotating beam fatigue tests this is a particular challenge, because specimen surfaces tend to rub and shear during final fracture, leading to surfaces that are often challenging to interpret.

## 3. Results and discussion

### *3.1. As-built witness coupon tensile tests*

As-built, 2-contour tensile bars were tested monotonically to failure to measure quasi-static mechanical properties. The minimum, maximum, and mean of 0.2% offset yield stress, elongation at failure and ultimate strength are given in Table 4 and show relatively low scatter and properties consistent with the manufacturer's experience with as-built IN718. This confirms that the material was manufactured within expectations, with limited uncertainty in print quality throughout. The tensile tests were conducted at a Nadcap-accredited testing laboratory using standard procedures. The complete data are included in the associated published dataset [17].

### *3.2. Heat treatment and recrystallization*

The heat treatment was confirmed to produce fully homogenized and recrystallized material, with the HIP treatment resulting in full density in all measured specimens. The lowest density measured across six specimens was 99.9998 % density. Representative inverse pole figure maps (face-centered cubic nickel with poles displayed parallel to Z) are shown in Figure 3. The figure shows roughly equiaxed grains with mean equivalent diameters of 69 µm in the X-Z plane and 61 µm in the X-Y plane.

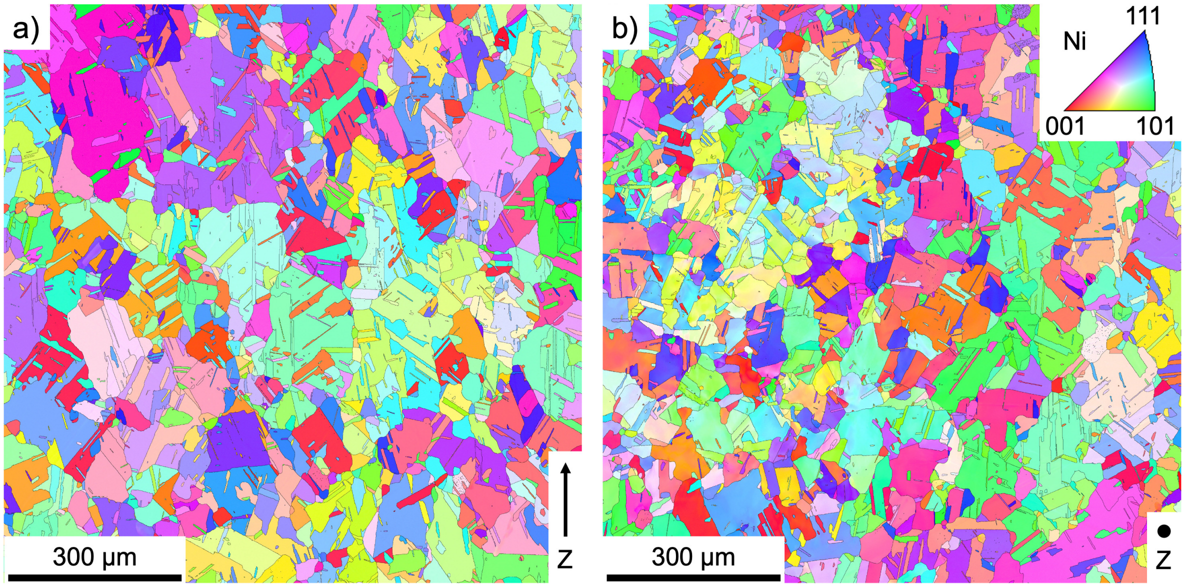

Figure 3: Representative EBSD map showing fully recrystallized and equiaxed grain structure after HIP and heat treatment, where Z indicates the build direction. a) X-Z plane, b) X-Y plane.

### *3.3. Evaluation of the as-built surfaces*

Optical images of the fatigue specimens in the final heat treated and machined state are shown in Figure 4 parts a)i), b)i) and c)i). Noticeably differences in surface finish appear photographs, corresponding to different numbers of contour passes. This change in luster was notable both before and after heat treatment. These optical differences are characteristic of the different surface features expressed by the surface generated by different numbers of contour passes. The specimens were also measured with X-ray CT. The 3D renderings of these measurements are shown in 3D in Figure 4a)ii)-c)ii). Only specimen surfaces are shown; no pores were observable at the voxel edge length of 4.5 µm that was used. The 3D renderings show a subset of the full 3D scan to more clearly show the surface features.

The data from X-ray CT were then also used to compute the surface feature depths, as outlined in Section 2.6. Figure 4d)-f) provide quantification to the observable differences in specimen luster and surface character. Two-contour surfaces shown in Figure 4 tend to be the smoothest, with relatively little deviation from the mean, both in terms of shortest and longest radii. The exception here is the tendency to have occasional larger fluctuations in the radius, which are observed in the X-ray CT images themselves, and are be caused by hemispherical material occlusions (see Figure 6). The 1-contour specimen profile reveals more deviations from the mean diameter than for the 2-contour condition, i.e., a slight shift rightwards of the black line. Similar to the 2-contour condition, occasional deep features are observed. However, for 1-contour, they do not appear as obviously differentiated from the bulk surface as in the 2-contour surface. The 0-contour surface has more rigorous features, with about three times the mean $S_v^{XCT}$ as the 1-contour condition.

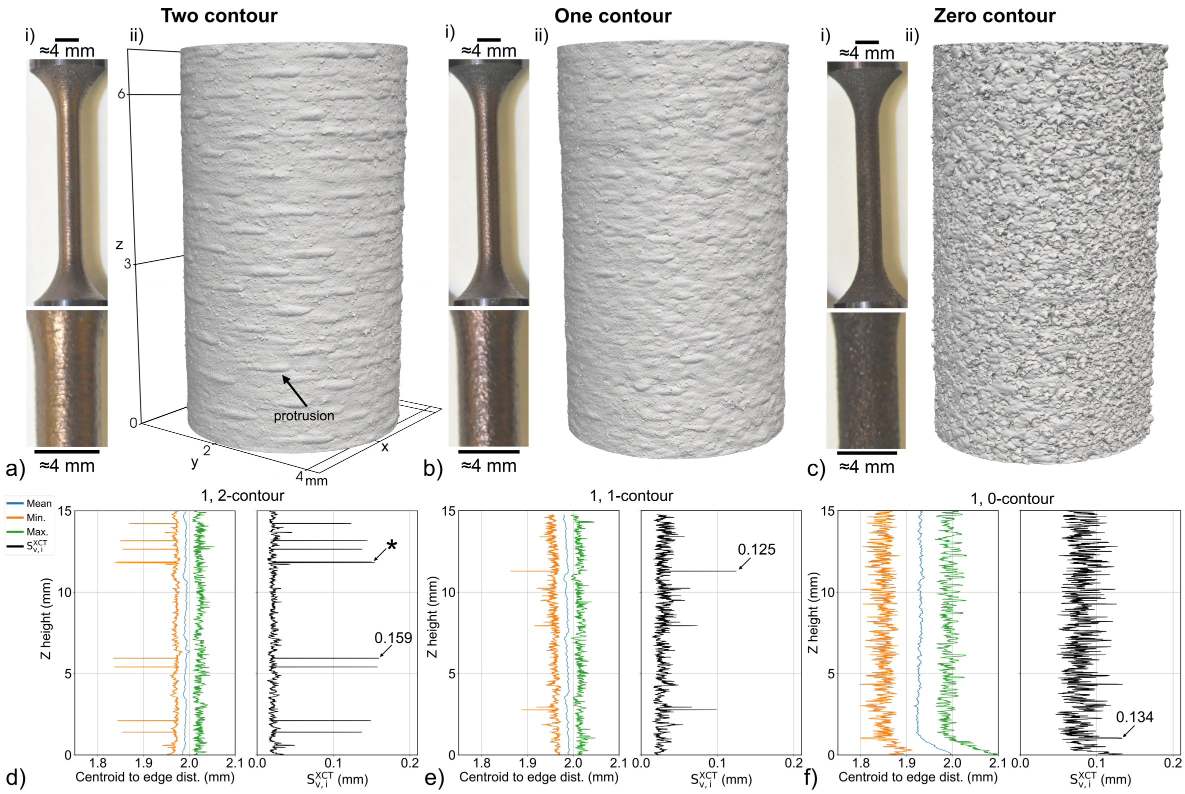


Figure 4: Surface measurements using X-ray CT of three example specimens (1.1, 1.2, 1.3). a)-c) are optical images (i's) and 3D renderings of X-ray CT reconstructions (ii's) of the outside surfaces, showing visible differences in surface morphology and luster: a) 2-contour, b) 1-contour, c) 0-contour. X-ray CT renderings are all the same size. d)-f) show their respective surface feature measurements, where the plot on the left shows the minimum, mean, and maximum extents found at each Z-height and the plot on the right shows the valley depth ($S_v^{XCT}$) computed from these values. d) 2-contour, e) 1-contour, and f) 0-contour. In d), the features that cause the peak in $S_v^{XCT}$ marked with an asterisk are shown in detail in Figure 6. Overall, decreasing the number of contours make the surface features trend deeper and less sporadic, although for 1-contour the maximum depth features observed (as indicated by an arrow and number) are not as deep as for 2-contour. These trends are summarized in Figure 5.

The surface feature observations are consistent across our specimens. To provide an example of this, summary analysis of locations 1 and 21 are provided in the violin plots in Figure 5. This demonstrates the differences in mean and spread of the $S_v^{XCT}$ across the number of contours. Looking across each row of Figure 5, the shaded region gradually shifts upwards, indicating an increase in mean $S_v^{XCT}$. The consistency of the measurement between replicates is demonstrated by the similarity within columns, e.g., comparing Figures 5a and 5d. The full plots, similar to Figure 4d-4f, for all six of these conditions is provided in Appendix C.

From these plots and X-ray CT images, we observed that rough surfaces possess reentrant and salient features with high aspect ratio, which cannot be fully captured by line-of-sight surface profilometry techniques. Although the spatial resolution of X-ray

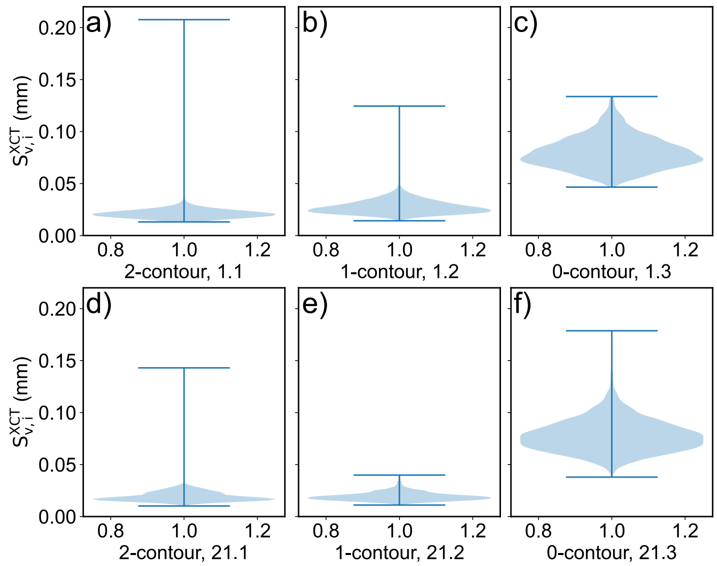


Figure 5: Violin plots showing the mean, spread, and range of $S_v^{XCT}$ for six specimens a) location 1, 2-contour, b) location 1, 1-contour, c) location 1, 0-contour, d) location 21, 2-contour, e) location 21, 1-contour, f) location 21, 0-contour. This visually demonstrates the change in overall mean surface feature depth and spread of depths along the height of the specimens and number of contour passes decreases. Replicate specimens are shown to demonstrate repeatability and consistency between locations on the build plate.

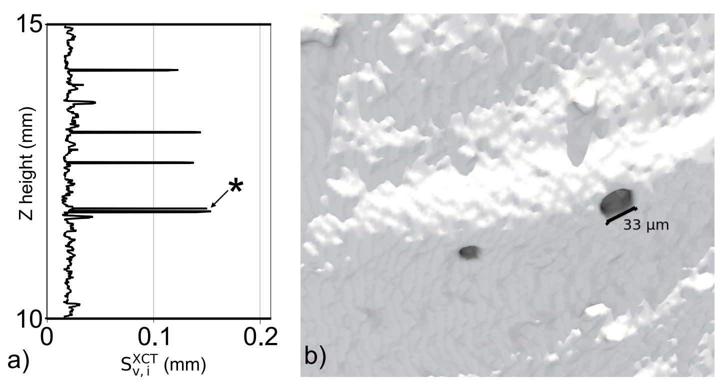


Figure 6: a) Peaks in $S_v^{XCT}$ showing two nearby peaks, marked with an asterisk, at about Z=11.82 mm, extracted from Figure 4d). b) a visualization of the specimen from X-ray CT, viewed at a semi-oblique angle, showing a pair of hole-like features which are responsible for the peaks in a).

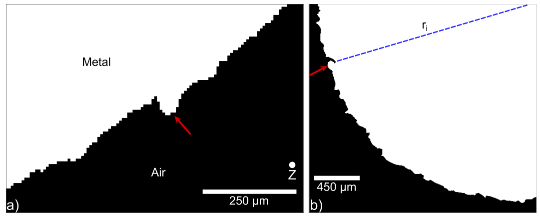


Figure 7: Example 2D image slices extracted from the X-ray CT data, showing a sub-set of the cross-section perpendicular to the gauge length. The image is segmented such that air is black and metal is white. a) specimen 1.2, 1-contour and b) specimen 1.3, 0-contour. Potential features that would be obfuscated by using only top-down topography measurement techniques are highlight by red arrows. The blue dashed line indicates the radius that would be used by the $S_v^{XCT}$ measurement.

CT is lower than, e.g., laser profilometry or focus variation microscopy, the complex topography of as-built surfaces necessitates such a full-3D characterization technique to accurately reproduce the surface morphology. Two slices exhibiting deeper surface features than would be accessible with line-of-sight measurements are shown in Figure 7; these types of features are particularly prevalent in the 0-contour condition (Figure 7b). This is a trade-off which must be considered when selecting an inspection technique. The lower resolution of X-ray CT means that the curvature of notch tips is less precisely measured, which would impact computed stress concentration factors from the images. However, deep surface connected features that are not visible with line-of-sight methods act as notches, which are important for fatigue damage initiation.

### *3.4. Stress-life fatigue testing results*

Fatigue lives of the tested specimens are plotted in terms of nominal maximum stress amplitude of the outside fiber of the cylinder $\sigma_a$ versus cycles to failure $N_f$ in Figure 8. The plots are constructed to show each possible pair of conditions. Points are be repeated between sub-figures, to enable comparison between different conditions. Populations of different surface condition are coded by marker color and marker shape, and runout specimens are represented with hollow icons. Runout is defined as a specimen with no failure after $1 \times 10^7$ cycles. To demonstrate the different trends, each set of points for given condition is fit using statistical techniques [20] to the equation

$$\log_{10}(N_f) = \beta_0 + \beta_1 S^{-\beta_2} + e, \tag{2}$$

where $N_f$ is the number of cycles to failure, the $\beta$ terms are model parameters. $S$ is the stress level, and $e$ is an error term that is assumed to be normally distributed with mean 0 and variance $\sigma_e^2$, which is itself a model parameter. Standard censored statistical analysis [20] was used to account for censoring runouts, and the parameter $\beta_2$ was determined to be 0.25 in an independent analysis and assumed to be known without error to simplify in the minimization used to identify the remaining model parameters for each condition. Note that this form is mathematically equivalent to the Stromeyer equation [21], but arranged to estimate uncertainty in the measurand ($N_f$). Note that assuming the $\beta_2$ parameter is known without error may slightly narrow the confidence bands, since the uncertainty from the exponent is not taken into account. From the statistical analysis, the 95% confidence bands and estimated model fit lines are extract and plotted along with the data points for each condition in Figure 8. The data has been compressed into one set of axes in Appendix D.

During testing, some amount of vibration in the specimens caused by minor warping or simply noise in the system resulted in fluctuations in the peak stresses applied. The magnitude of these fluctuations is represented by the range bars on the plot. Note that it maybe perhaps be more appropriate to consider the stress amplitude that of the upper end of the range bar rather than the simple nominal test value, as it is likely that the failure is driven by maximum stresses rather than mean stresses. However, because this would be non-standard, the nominal mean stress was used in the statistical analysis. Additionally, the stress variability was not propagated through the uncertainty estimates for $N_f$ which may decrease the predicted uncertainty.

The analysis shows that there are no statistically significant differences ($p > 0.05$) between the slopes and intercepts of any conditions save for the polished condition, which is different from the other conditions. This is made visually apparent in Figure 8. In each of Figures 8b, 8d, and 8f the confidence bands overlap, while for those plotting polished versus unpolished conditions 8a, 8c, and 8e largely do not, with the exception of 8e (however, the it was still shown to be significantly different). The relatively broad 95% confidence bands, and the corresponding lack of statistically significant differences between the SN curves for any of the as-built surface conditions, could very well be a result of the limited number of specimens and repeats present in our data. Thus, although differences may in fact exist, with the present data we are unable to say that statistically significant differences exist between the different number of contours in terms of fatigue life. Further work would be necessary to fully illuminate this. For more direct comparison of all four conditions, the points are replotted all on the same axes in Figure D.17.

Although reasonable precautions were taken, per ASTM testing standards [12], there may be residual stresses present due to machining the surface of the polished specimens. It is possible, although we think unlikely, that the fatigue strength of the polished condition has been increased by induced compressive surface stresses from the machining and polishing steps, which has caused this difference. More likely, in our estimation, is the introduction of local stress raisers in the form of surface irregularities in the non-polished conditions.

In high cycle fatigue literature, rigorous statistical analysis is somewhat uncommon due to the difficultly of obtaining statistically relevant number of tests. Often, perceived differences between SN data based on relatively few data points are deemed sufficient to identify interesting trends. Under this less exacting standard of evidence, we note that in some cases only the far bounds of the confidence bands overlap. Specifically, for 0-contour compared to 1- and 2-contour there seems to be an decrease fatigue strength at $10^7$ cycles. There is a mild decrease in fatigue strength at $10^7$ cycles from 2-contour to 1-contour as well, although the data substantially overlap. Specifically, the model for 0-contour crosses $10^7$ at about 205 MPa, the 1-contour model cross the same point at

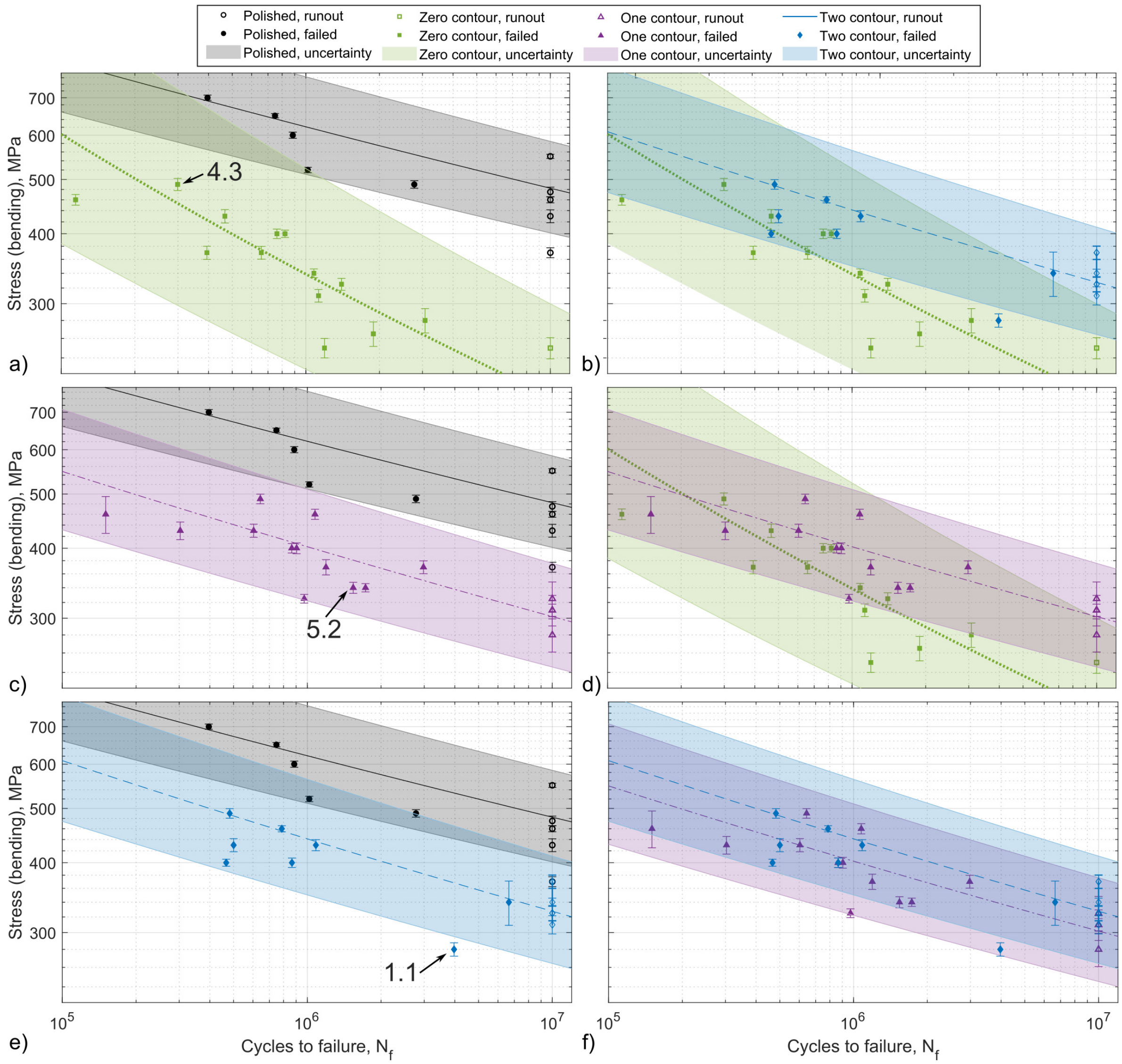


Figure 8: Stress amplitude versus life curve for four different surface conditions: fully polished, 2-contour, 1-contour, and 0-contour. Mean applied stress is plotted as the center point and the error bars represent the maximum fluctuations in stress during the test. This shows the differences and overlaps between conditions. a) Polished and zero-contour, b) zero-contour and two-contour, c) polished and one-contour, d) zero-contour and one-contour, e) polished and two-contour, f) one-contour and two-contour. Note that the axes are shared where possible. In a), c) and e) specimens selected for more detailed fractographic analysis are noted.

301 MPa, and the 2-contour at 328 MPa. The difference between maximum (2-contour) and minimum (0-contour) modeled fatigue strength at $10^6$ cycles is 101 MPa. At $10^5$ cycles, the trend reverses and 1-contour is the lowest at 549 MPa, while 0-contour and 2-contour are 602 MPa and 609 MPa respectively. Although statistically insignificant, these suggests that more thorough SN-curve development may find meaningful differences, if the modeled spread ($\sigma_e$) is being increased due to limit data points (i.e., our sample standard deviation is broader than the true population standard deviation). In particular, between the slopes of the 0-contour and 1- and 2-contour conditions, which the current data is insufficient to prove. Put another way, at higher stresses, e.g., above 450 MPa there maybe greater similarity between the apparent fatigue life as a function of number of contours than at lower stress, although this has not been proven statistically with the current data (i.e., the confidence bands overlap throughout the curves in Figure 8b and 8d).

### *3.5. Fractographic analysis*

The fracture surface for specimen 1.1 is shown in Figure 9, at three different levels of detail. This specimen is somewhat unique in that it failed earlier than other specimens with similar, relatively low, applied stress. However, there are no completely clear indicators on the fracture surface to indicate why—it has multiple initiation sites, with one dominating and eventually leading to failure. The primary site is shown in detail in Figures 9b) and 9c), and appears to be a notch-like crevice underneath a partially attached powder particle. Unfortunately, this fracture surface is just outside the extent of the X-ray CT scan, as this scan missed part of the very top of the gauge section where failure occurred. Despite being somewhat lower stress than the other 2-contour failed specimens, this type of fracture surface is typical of the 2-contour condition.

Figure 10 demonstrates a representative 1-contour failure surface, that of specimen 5.2, which exhibited a fatigue life similar the other 1-contour specimen tested at 340 MPa. In other words, it is not an outlier, unlike specimen 1.1. In Specimen 5.2, a single feature was the predominant driver of failure. Fatigue striations appear on a relatively planar surface (compared to the failure site in, e.g., 1.1 or 4.3) in sub-Figure 10d), which may be indicative of a poorly-oriented grain, which was an initiation site. This forms a patch of apparently different fracture surfaces at the edge of the material, with the bottom of Figure 10c) showing what may have been surface notch or other stress raiser adjacent to this grain.

The fracture surface of a 0-contour specimen, 4.3 shown in Figure 11, has distinctly different surface-connected features than for the specimens with contour passes. In this case, repeated similar notches appear at roughly the spacing of the hatch (orange arrows), which may be indicative of lack-of-fusion type defects near the ends of the scan lines during the build. In the 0-contour case, tracks terminate at the surface, making this a possible sources of surface-connected defects although the precise cause of these features would require further investigation. These features appear to have been the cause of failure, as indicated by the fatigue markings in Figure 11d), although this specimen is typical within the stress-life context.

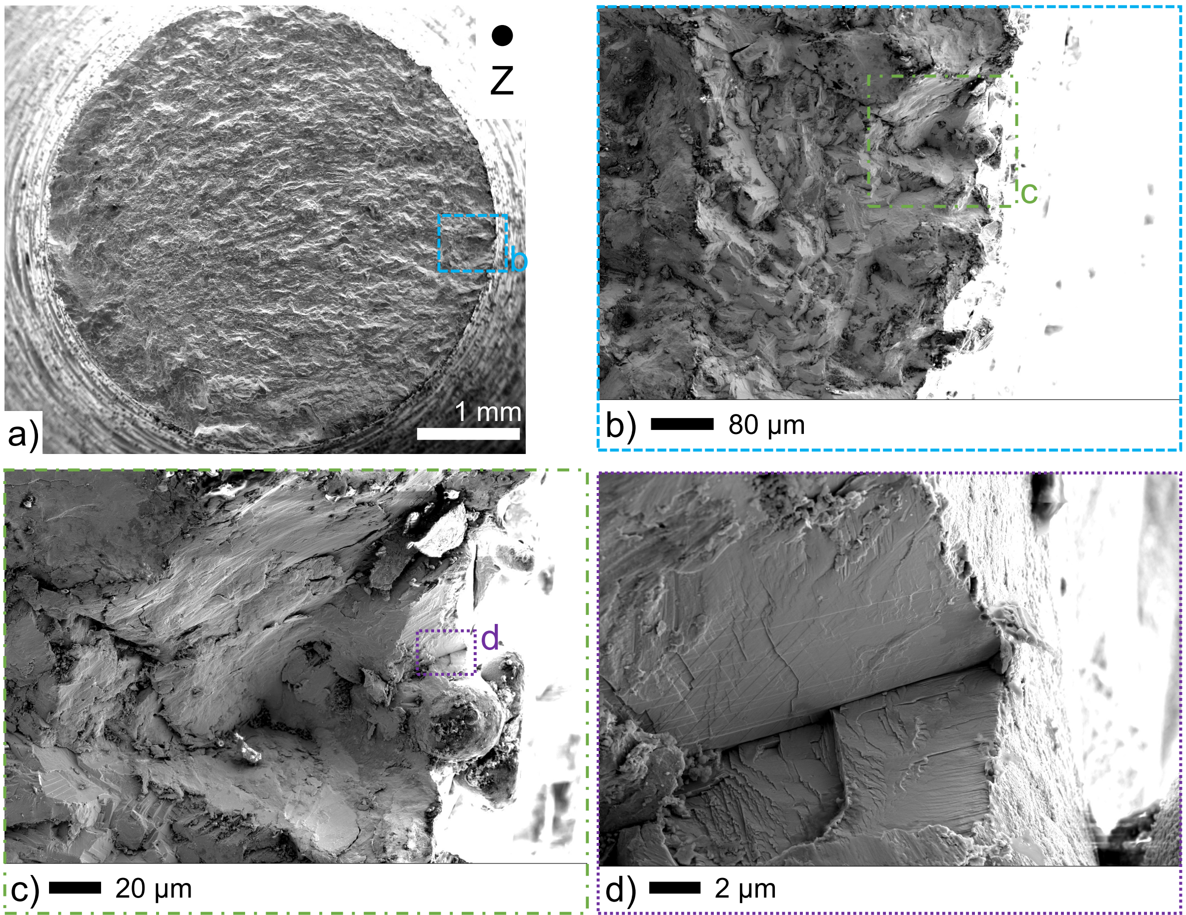


Figure 9: SEM micrographs of the fracture surface of specimen 1.1 (2-contour), with progressively increasing levels of magnification. a) the full fracture surface; b) a likely initiation site as outlined in blue in a); c) a detailed image of the site highlighted in green in c); and d) shows region in purple in c), highlighting cleavage along planar surfaces. Failure was driven along a notch-like feature underneath a partially attached powder particle. a) shows multiple initiation sites, only one of which is explored in detail. This specimen was tested at 280 MPa with failure at $N_f = 3\,971\,350$ cycles.

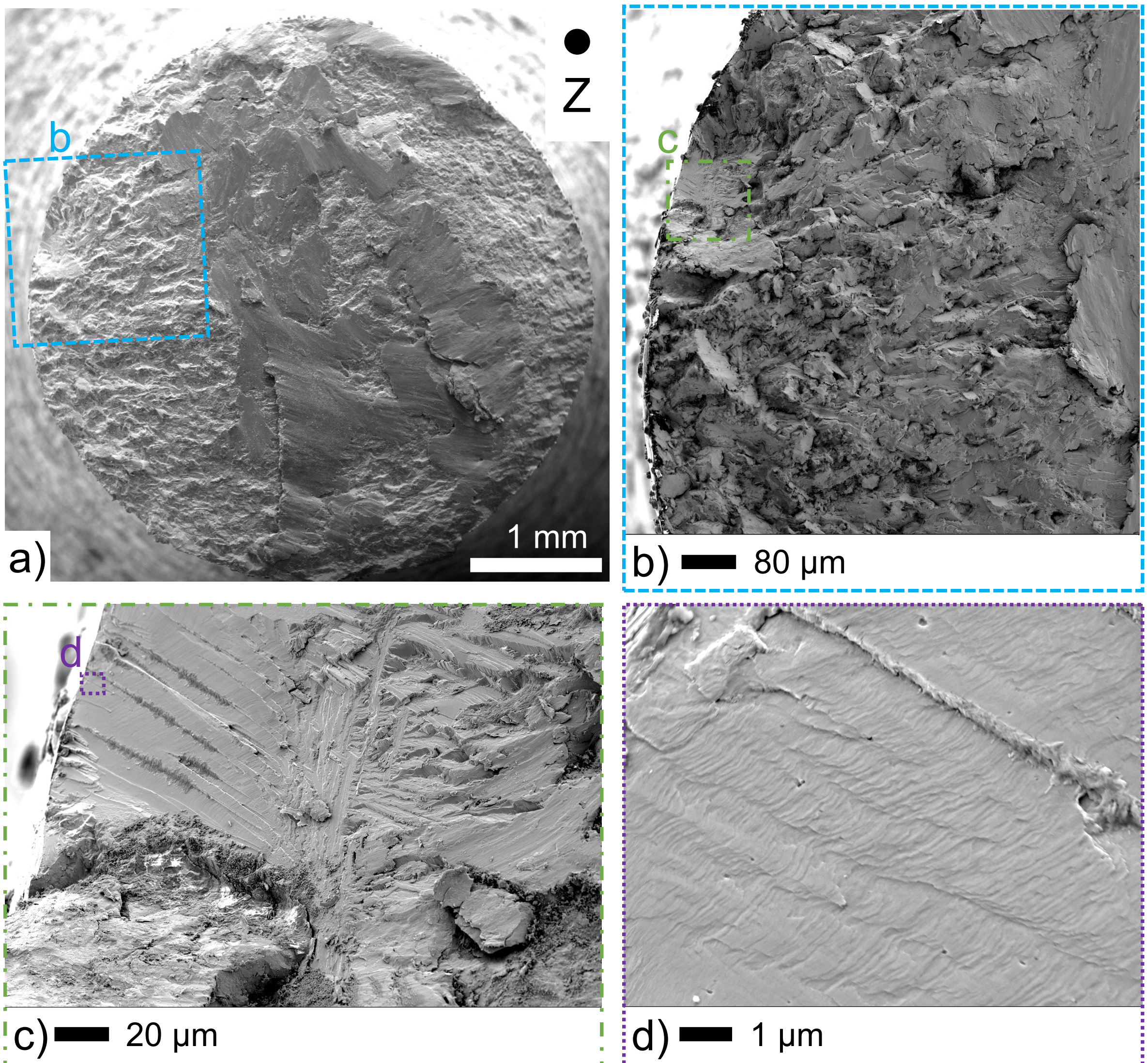


Figure 10: SEM micrographs of the fracture surface of specimen 5.2, a 1-contour example, with progressively increasing level of detail. a) full failure surface, with a fracture pattern indicating emanation from the left edge with the field of view of b shown in a dashed box, b) the edge site in more detail, c) a planar feature at the failure site, with d) fatigue striations likely along a crystallography slip plane. Stress was 340 MPa and $N_f$ =1 539 262 cycles.

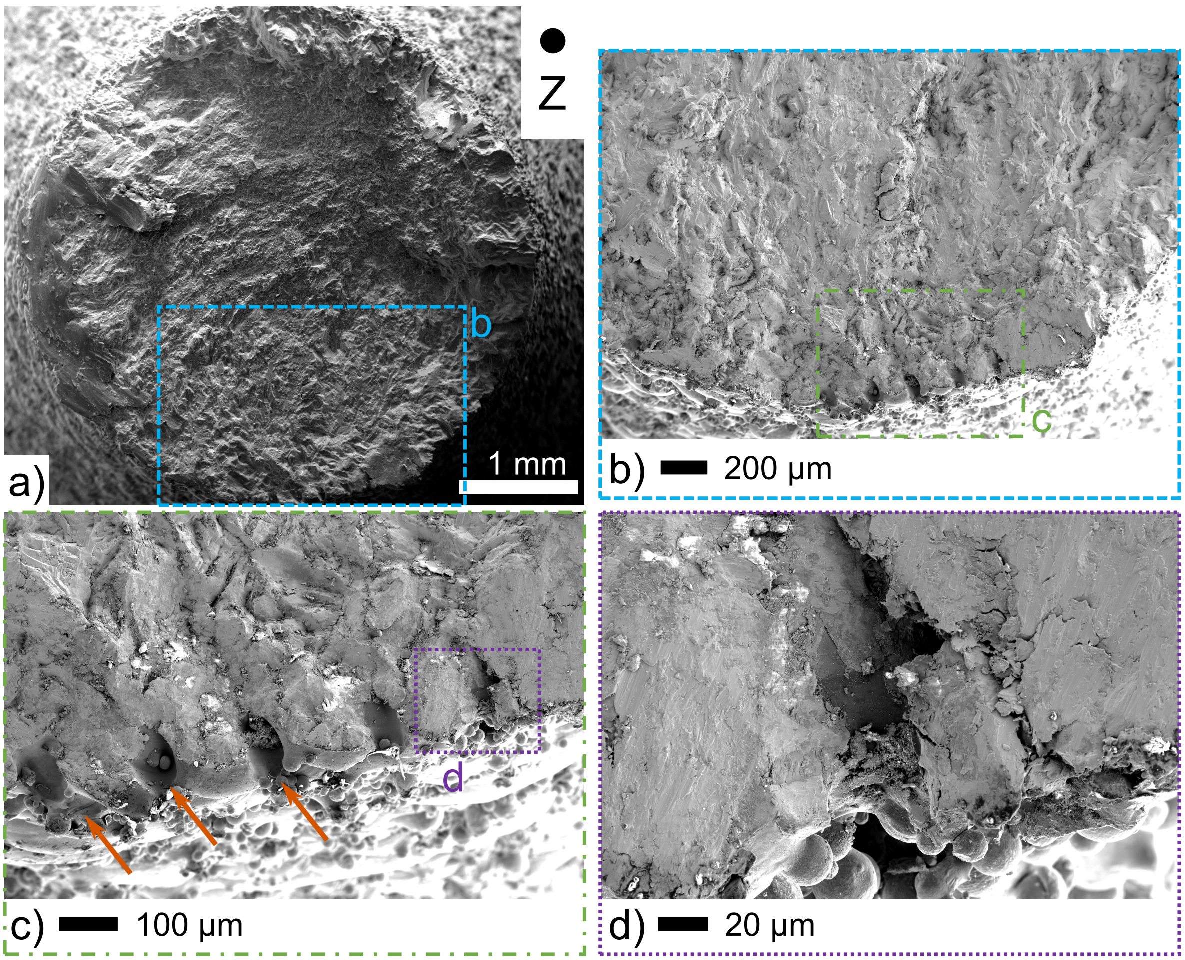


Figure 11: SEM micrographs for specimen 4.3, a 0-contour example tested at 490 MPa with failure at $N_f$ =298 955 cycles. a) the full fracture surface, and b) the failure site in context of a larger region. c) failure site, with large surface-connected holes at roughly the hatch spacing (orange arrows), potentially lack-of-fusion where the hatch is exposed to the surface. d) detail of one of these holes, showing likely fatigue failure surface.

Observations of the fracture surfaces across all specimen classes indicate that multiple initiation sites are common across conditions. We hypothesis that a mix of surface-driven initiation and crystallography-governed crack initiation and growth is the likely mechanism of failure: cracks initiate at stress raisers at or near the surface (where surface is defined as the air/metal interface), and begin propagating within the local crystallographic environment, forming the striations seen in, e.g., Figure 10d). Because this growth may be relatively slow, and slowed further as the crack propagates inwards and away from the peak stress caused by bending, other cracks may being to grow and the depth of notch may not have as much importance as they would under axial loading [22]; this would increase the likelihood of multiple initiation sites being observable on the failure surface. This mechanism is further promoted by the characteristic size of the first-order microstructure (i.e., grains) being similar to that of the surface features, both being of approximate order 100 µm.

One possible explanation for the convergence of stress-life results at higher stresses compared to the greater separation (although still within overlapping 95% confidence bands) relates to this proposed mechanism. At lower stresses, initiation of a crack may require the convergence of both a notch-like feature acting as a stress raiser at the surface as well as an underlying grain oriented such that plastic slip is more favorable. At lower applied stress, the initiating forces may be too low to overcome slip resistance if only one factor is present. The convergence of a geometry and crystallographic stress raiser may be necessary to drive significant enough dislocation motion to result in pile-up (e.g., formation of persistent slip bands) and eventual crack initiation either at a surface features or a grain boundary interface. For the more-contour and smoother surface conditions, fewer stress raiser exist and thus the probability of this convergence of these two factors is lower. This lower chance leads to generally longer lives (with a few notable outliers). Conversely, at higher stresses, it may be that any stress raiser (or unfavorably oriented grain) is enough to drive significant enough dislocation motion to initiate a crack. In other words, the local grain orientation is less important. The X-ray CT data shows that geometric stress raisers are present in all contour conditions implying fracture may initiate and grow similarly at the higher stresses where a geometric stress raiser is sufficient to drive initiation, with variations mostly upon the specifics of individual specimens, rather than different mechanisms leading to different necessary and sufficient conditions for initiation to occur. Although these mechanisms seem plausible, in future more direct interrogation of the behavior, e.g. through crystal plasticity modelling, could help confirm if this is the correct interpretation.

To illustrate the finding that deepest or otherwise noteworthy surface features are not necessarily located at the failure site, Figure 12 shows one initiation site for the 0-contour, specimen 21 (i.e., 21.3) as imaged using SEM. This shows the failure site location in the overall failure surface, as well as detailed views of the feature from which the crack propagates. Classical fatigue striations are present, shown in detail in Figure 12d). The same specimen imaged before testing with X-ray CT and after testing with SEM is presented in Figure 13. In Figure 13, we identify the specific failure site shown in Figure 12 in the surface profile plot with a red arrow; clearly, this

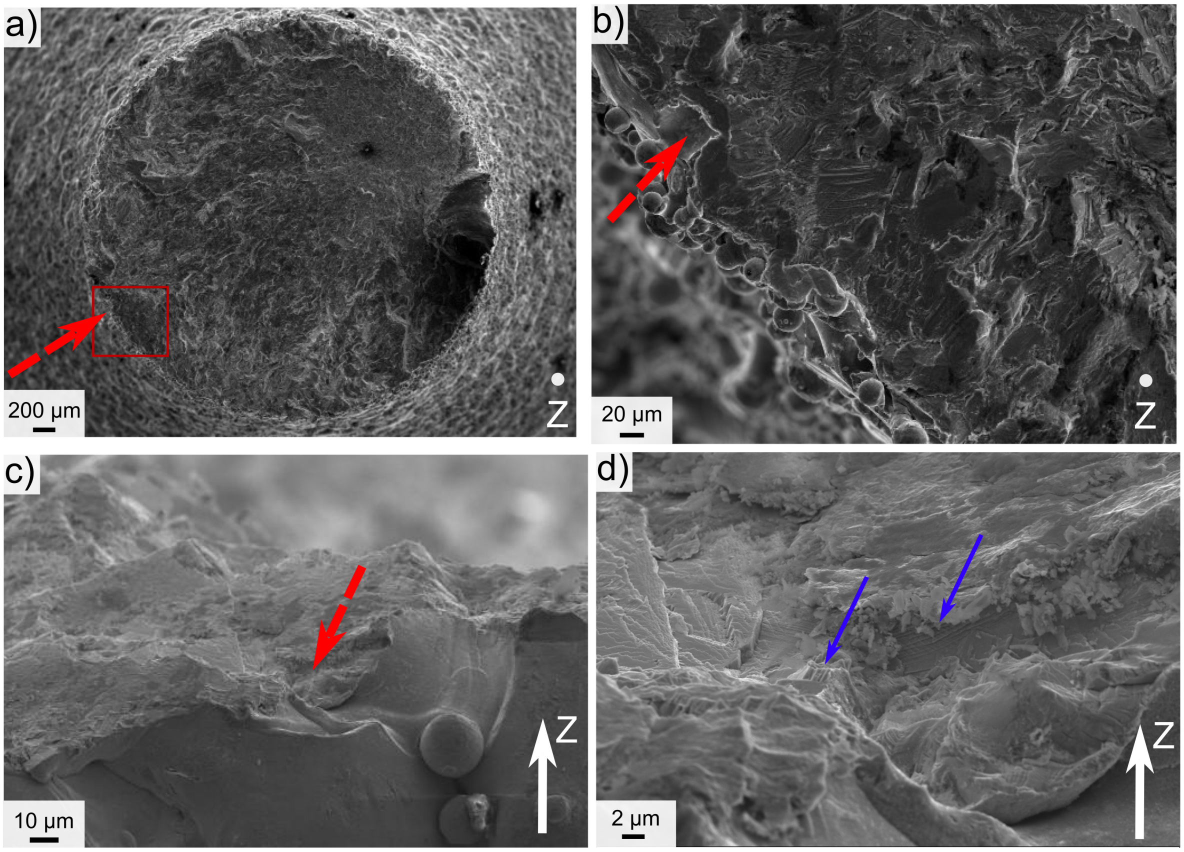


Figure 12: SEM micrographs of the fracture surface for specimen 21.3; a) full fracture surface, with detail highlighting the region shown in b), the local region from a top-down perspective that appears to be an initiation site; c) shows an edge-on view of that site, highlighting the nearby notch; finally, part d) zooms in on the material just behind the notch shown in c), and highlights striations (blue arrows) indicative of fatigue progression. From this, it appears this site is at least one of the initiation sites.

is not the deepest surface feature. To confirm the shape and location of the feature, the right two panes of Figure 13 demonstrate matching SEM and X-ray CT features, with color-coded arrows highlighting unique features that can be used as fiducial markers to visually identify the failure location (marked with a red semi-dashed arrow). Finally, the bottom left pane shows the deepest feature identified. Somewhat obscured by the resolution of the X-ray CT rendering, this appears to be a surface-connected pore-like feature buried relatively deeply. This feature is not near the eventual failure site, as indicated by the distance in Z-height between the red and orange arrows in Figure 13a). Although at the same nominal stress level, this deeper, sharper feature did not result in failure.

It is understood that the deepest notch may not be the best measure for L-PBF surfaces, especially when used to correlate to fatigue performance. However, the deepest notch measurement is appealing in its simplicity and, using 2D or quasi-3D measurements such as profilometry, ease of measurement. Classically, $S_v$ has been used as a

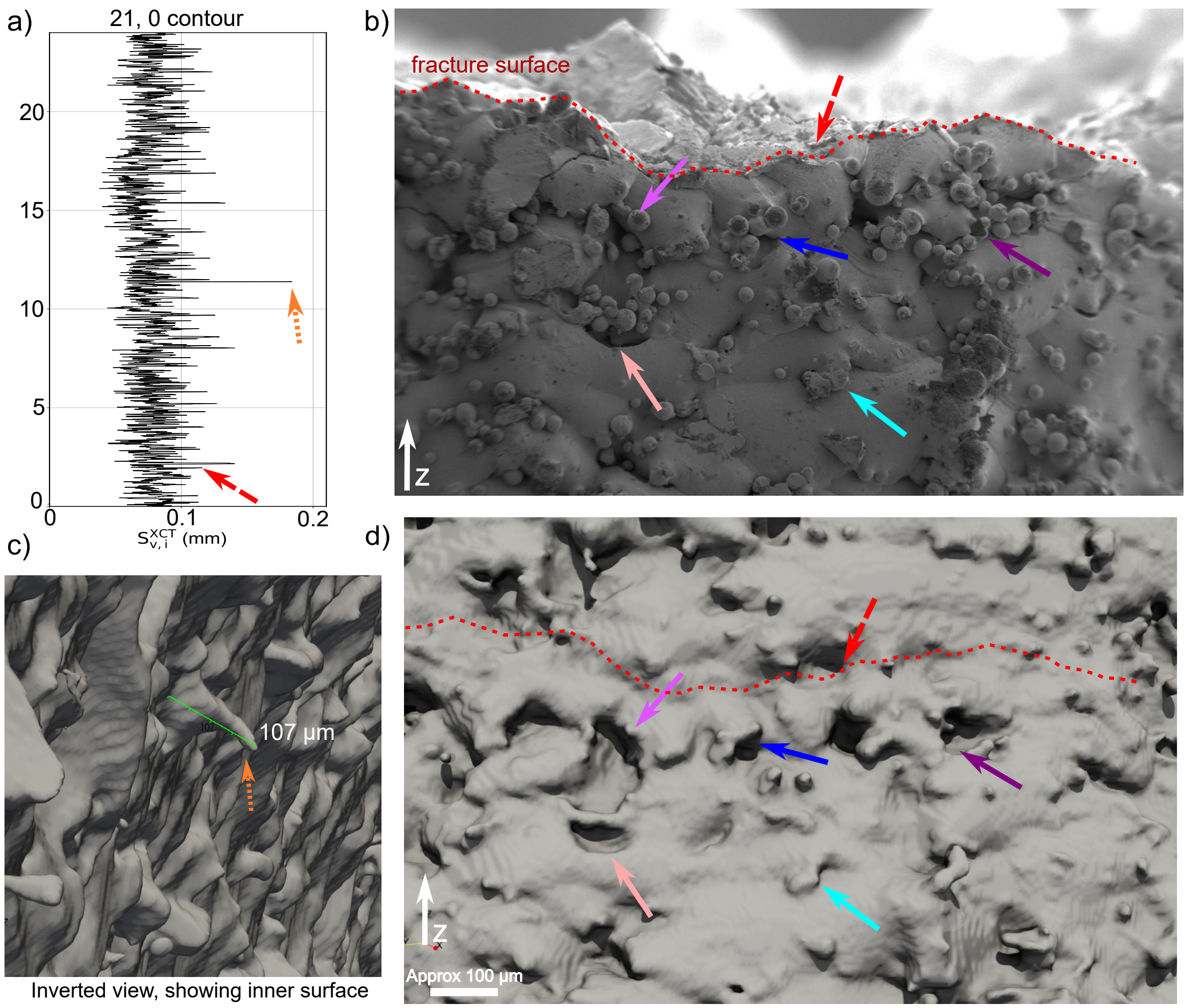


Figure 13: The surface profile (a) annotated with two different 3D surfaces that cause the features shown in the profile. The right side panes show matching SEM of the failure site (b) explained in Figure 12 with X-ray CT pre-failure of the same region (d). In b) and d) the dashed line was added to emphasize the fracture path; the location of the dashed red arrows match that in (a). The failure site itself (red dashed arrow) is not particularly notable from its surroundings in the X-ray CT rendering. The deepest notch (dotted orange arrow), which despite being relatively sharp did not cause failure, is rendered in the lower left pane (d). The colored arrows shown on both b) and d) indicate unique features used as fiducial markers to confirm the two locations are identical. This demonstrates that only using surface features and profiles may not be sufficient to correlate with fatigue performance.

surface profile quantification for more regular surfaces, and has thus seem some use for AM surfaces as the field develops. Here, we have focused on notch depth to outline a case against its simplistic use. In general, more robust and mathematically descriptive parameters ought to be obtained for AM surfaces. For instance, concepts such as tortuously (such as is used in geological and biological applications), projected area (as in the Murikami approach), or feature sharpness may be better criteria. Mathematically describing AM surfaces, ideally in 3D such as with X-ray CT data, using more sophisticated parameterization is an promising avenue for future work.

## 4. Summary, Conclusions, and Future Work

IN718 fatigue coupons were built using L-PBF to test the impacts of different numbers of contour passes, and thus surface characteristics, on the fatigue life. This study was designed to isolate changes in surfaces as specifically as possible, by controlling as many other factors as possible that may impact fatigue life. Specimens with 0, 1, and 2 contour passes, as well as fully machined and polished specimens, were tested in the high-cycle fatigue regime after a full heat treatment using rotating bending fatigue. Note that this work is limited to vertically oriented specimens; the impacts of different contouring may be different for different wall angles. Including surfaces with different wall angles in this study would have made isolation of variables, and thus interpretation of results, much more challenging, but could be attempted in future work. X-ray computed tomography was used to analyze surface features in the as-built surfaces, indicating that a few deep features appear in all specimens, but more complex and deeper features appear for fewer contour passes. Fracture surfaces indicated multiple initiation sites in many cases, with cracks propagating along planar features, likely slip planes. The use of X-ray CT enabled observation of the deepest penetrating surface features despite overhanging material or sharp notches, which traditional top-down surface metrology techniques would be unable to capture. Using this, our study determined that the shortest centroid-to-surface radius was not necessarily the fatigue initiating site. Although the deepest notch criterion was not found to be correlative, this overall feature-specific perspective on surface-related AM fatigue may be helpful to consider when developing new industrial screening processes for part quality.

Rough surfaces of all types tends to decrease fatigue life and overall fatigue performance in these specimens, when compared to specimens with polished surfaces. No statistically significant differences in fatigue life of specimens with surfaces processed with different number of contour passes was identified. Of practical interest at lower confidence than 95% there may be a difference between 0-contour behavior at relatively higher numbers of cycles (i.e., above $10^6$) and the other two conditions. Meanwhile, 1-contour and 2-contour remain quite similar even with this lowered standard of evidence. This suggests that further studies may be worthwhile to attempt to prove that while 1-contour adds to the fatigue strength at $10^7$ cycles, the gain in fatigue strength achieved by adding a second contour pass is more marginal.

By using combined SEM and pre-test X-ray CT datasets, we demonstrated that a perspective of deepest, or even near-deepest surface feature, may be insufficient to correlate to high cycle fatigue performance. This has important implications, as some substantial effort has been made to correlate typical surface roughness parameters, such as $S_v$, to fatigue life. Because we found that final failure sites are not initiated at the deepest surface features, our work suggests that other factors (crystallography, residual stresses, notch sharpness or area, etc.) may be necessary to include in models predicting material performance with as-built surfaces. More work is required to understand what exactly constitutes a so-called killer defect, because deepest surface notch cannot necessarily be relied upon as the failure site.

A future study will be designed to collect more localized measurements, i.e., on the scale of individual grains, to further test the theory that grains and notches are both important at lower stress levels. This will involve specifically designed experiments allowing for direct observation of notches (with SEM and X-ray CT) and grains (with EBSD or other diffraction-based methods, perhaps high-energy diffraction microscopy) in the vicinity of the failure site at higher resolution than was achieved in the current work. To supplement this, mechanistic computational crystal plasticity simulations to deduce relative impacts of specific grain orientation and notch shape under bending loads are planned. Other planned works will report on the impact of layer height and the use of multiple concurrent lasers on the surface feature and fatigue life.

## Data availability

All codes and data used in this manuscript are made freely and publicly available via NIST's data publishing Public Data Record mechanism under Ref. [17] for the dataset and under Ref. [18] for the image processing codes.


## Acknowledgments

Christopher N. James at Metalex Thermal Specialties in Berthoud, CO is acknowledged for performing the vacuum furnace heat treatments in this work (stress relief, solution, and age).


## CREDiT contributions

**OLK:** conceptualization, methodology, software, investigation, data curation, writing - original draft, visualization, supervision, project administration, funding acquisition.
**JTB:** conceptualization, methodology, investigation, writing - review & editing, visualization.
**ND:** investigation, writing - review & editing, visualization.
**PS:** conceptualization, investigation (AM builds), visualization.
**LK:** investigation (statistics analysis), formal analysis.
**CB:** resources, investigation (heat treatments), funding acquisition.

**DG:** conceptualization, resources, supervision, funding acquisition.
**NH:** conceptualization, validation, writing - review & editing, resources, supervision, funding acquisition.

## Conflicts of Interest

PS and DG are employed by SLM Solutions, the makers of the AM machines and material tested, but were not involved in the analysis and testing of said material after production. No other authors report possible conflicts.

## References


[1] E. Maleki, S. Bagherifard, M. Bandini, M. Guagliano, Surface post-treatments for metal additive manufacturing: Progress, challenges, and opportunities, Additive Manufacturing 37 (2021) 101619. doi:10.1016/j.addma.2020.101619.

[2] J. C. Snyder, K. A. Thole, Understanding Laser Powder Bed Fusion Surface Roughness, Journal of Manufacturing Science and Engineering 142 (2020). doi:10.1115/1.4046504.

[3] J. C. Fox, A. L. Pintar, Prediction of Extreme Value Areal Parameters in Laser Powder Bed Fusion of Nickel Superalloy 625, Surface Topography: Metrology and Properties 9 (2021) 025033. doi:10.1088/2051-672X/ac0061.

[4] E. Sadeghi, P. Karimi, R. Esmaeilizadeh, F. Berto, S. Shao, J. Moverare, E. Toyserkani, N. Shamsaei, A state-of-the-art review on fatigue performance of powder bed fusion-built alloy 718, Progress in Materials Science 133 (2023) 101066. doi:https://doi.org/10.1016/j.pmatsci.2022.101066.

[5] J. Gockel, L. Sheridan, B. Koerper, B. Whip, The influence of additive manufacturing processing parameters on surface roughness and fatigue life, International Journal of Fatigue 124 (2019) 380–388. doi:10.1016/j.ijfatigue.2019.03.025.

[6] D. B. Witkin, D. Patel, T. V. Albright, G. E. Bean, T. McLouth, Influence of surface conditions and specimen orientation on high cycle fatigue properties of inconel 718 prepared by laser powder bed fusion, International Journal of Fatigue 132 (2020) 105392. doi:10.1016/j.ijfatigue.2019.105392.

[7] R. Konečná, G. Nicoletto, On the link between as-built surface quality and fatigue behavior of additively manufactured inconel 718, Procedia Structural Integrity 23 (2019) 384–389. doi:https://doi.org/10.1016/j.prostr.2020.01.117, 9th International Conference Materials Structure & Micromechanics of Fracture (MSMF9).

[8] G. Nicoletto, Smooth and notch fatigue behavior of selectively laser melted inconel 718 with as-built surfaces, International Journal of Fatigue 128 (2019) 105211. doi:https://doi.org/10.1016/j.ijfatigue.2019.105211.

[9] K. Solberg, F. Berto, The effect of defects and notches in quasi-static and fatigue loading of inconel 718 specimens produced by selective laser melting, International Journal of Fatigue 137 (2020) 105637. doi:10.1016/j.ijfatigue.2020.105637.

[10] A. R. Balachandramurthi, J. Moverare, N. Dixit, R. Pederson, Influence of defects and as-built surface roughness on fatigue properties of additively manufactured alloy 718, Materials Science and Engineering: A 735 (2018) 463–474. doi:https://doi.org/10.1016/j.msea.2018.08.072.

[11] S. Lee, S. Shao, D. N. Wells, M. Zetek, M. Kepka, N. Shamsaei, Fatigue behavior and modeling of additively manufactured in718: The effect of surface treatments and surface measurement techniques, Journal of Materials Processing Technology 302 (2022) 117475. doi:https://doi.org/10.1016/j.jmatprotec.2021.117475.

[12] E08 Committee, Practice for Conducting Force Controlled Constant Amplitude Axial Fatigue Tests of Metallic Materials, Technical Report, ASTM International, 2021. doi:10.1520/E0466-15.

[13] ASTM International, Additive Manufacturing Standards - Standards Products - Standards & Publications - Products & Services, 2023.

[14] F42 Committee, Specification for Additive Manufacturing Nickel Alloy (UNS N07718) with Powder Bed Fusion, Technical Report, ASTM International, 2021. doi:10.1520/F3055-14A.

[15] T. C. I. 164, Metallic materials — Rotating bar bending fatigue testing, Technical Report, International Organization for Standardization, 2010.

[16] SAE Internation, Heat Treatment: Nickel Alloy and Cobalt Alloy Parts, Technical Report AMS2774G, SAE International, 2020.

[17] O. L. Kafka, J. Benzing, N. Derimow, P. Schumacher, L. Koepke, C. Beamer, D. Godfrey, N. Hrabe, Effects of as-built surface with varying number of contour passes on high-cycle fatigue behavior of additively manufactured nickel alloy 718, 2023. doi:https://doi.org/10.18434/mds2-3044.

[18] N. H. Moser, O. L. Kafka, A. Landauer, IMPPy3D: 3D X-ray Computed Tomography Image Processing in Python, 2023. URL: https://github.com/usnistgov/imppy3d. doi:https://doi.org/10.18434/mds2-2806.

[19] S. van der Walt, J. L. Schönberger, J. Nunez-Iglesias, F. Boulogne, J. D. Warner, N. Yager, E. Gouillart, T. Yu, the scikit-image contributors, scikit-image: image processing in Python, PeerJ 2 (2014) e453. URL: https://doi.org/10.7717/peerj.453. doi:10.7717/peerj.453.

[20] W. Q. Meeker, L. A. Escobar, Statistical Methods for Reliability Data, Wiley, 1998.

[21] C. Stromeyer, The determination of fatigue limits under alternating stress conditions, Proceedings of the Royal Society of London. Series A, Containing Papers of a Mathematical and Physical Character 90 (1914) 411–425.

[22] R. Shrestha, J. Simsiriwong, N. Shamsaei, Fatigue behavior of additive manufactured 316L stainless steel under axial versus rotating-bending loading: Synergistic effects of stress gradient, surface roughness, and volumetric defects, International Journal of Fatigue 144 (2021) 106063. doi:10.1016/j.ijfatigue.2020.106063.

## Appendix A. Preliminary variable isolation study

To ensure as many confounding variables as possible were eliminated from the build layout and specimen design we conducted several preliminary experiments. We ensured that differences in surface roughness exist between the conditions, and that these differences are more than the differences between orientations with respect to the recoat and gas flow directions. We also checked that the number of contours does not substantially impact the final dimensions, to the extent that it would impact the fatigue tests. Mean dimensional deviation across all contour numbers for quantity $n = 18$ test blocks was 12.3 µm (standard deviation of 8.0 µm, across $n = 6$ specimens) in the x-dimension and 15.8 µm in the y-dimension (standard deviation 19.5 µm, $n = 6$). Part density was measured to be quite high (>99.85 % dense) even before HIP. Summary results are presented below, and the full data are included in the associated data publication [17]. This provided confidence that the only impact would be the number of contour passes, when the specimens were built vertically (i.e., the long axis is aligned with the build direction).

A preliminary build (Figure A.14) was used to assess three different factors that could possibly impact the planned study of the impact of number of contours on surface roughness for this study. First, we measured the density (using microscopy) of blocks made with the three different contour patterns (Figure A.15a). Second, we measured the surface roughness of the four sides of the blocks, to determine if there were measurable differences between faces along the gas flow or recoater directions (Figure A.15b). Third, the dimensional differences from the nominal (programmed) cube sizes were measured for each condition in two directions, $x$ and $y$. The blocks were 15 mm × 15 mm × 25 mm, and quantity $n = 6$ for all cases.

All three measures indicate that vertical builds would produce comparable results, able to isolate the impact of number of contours. Note, the long, narrow blocks on this build plate were used for a simultaneous study of IN718 heat treatments.

## Appendix B. Polishing steps [15, 12]

1. In the final stages of machining, remove material in small amounts until 0.125 mm of excess material remains.
2. Remove the next 0.1 mm of gage diameter by cylindrical grinding at a rate of no more than 0.005 mm/pass.
3. Remove the final 0.025 mm by polishing longitudinally to impart a maximum surface roughness of 0.2 µm Ra, in the longitudinal direction.
4. After polishing all remaining grinding and polishing marks should be longitudinal. No circumferential machining should be evident when viewed at approximately 20× magnification under a light microscope.
5. Degrease the finished specimen.

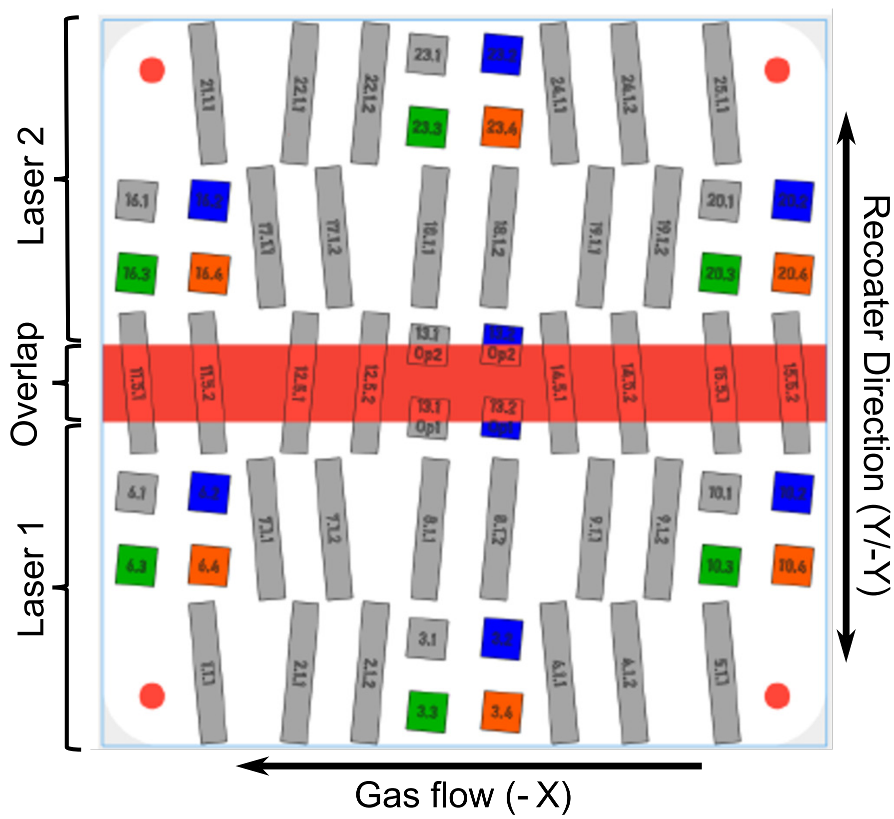


Figure A.14: Build layout for the preliminary study of density, size, and surface roughness. Note that only the square (in the top-down view shown) specimens were used here, the rectangles were used in a simultaneous study of different heat treatments.

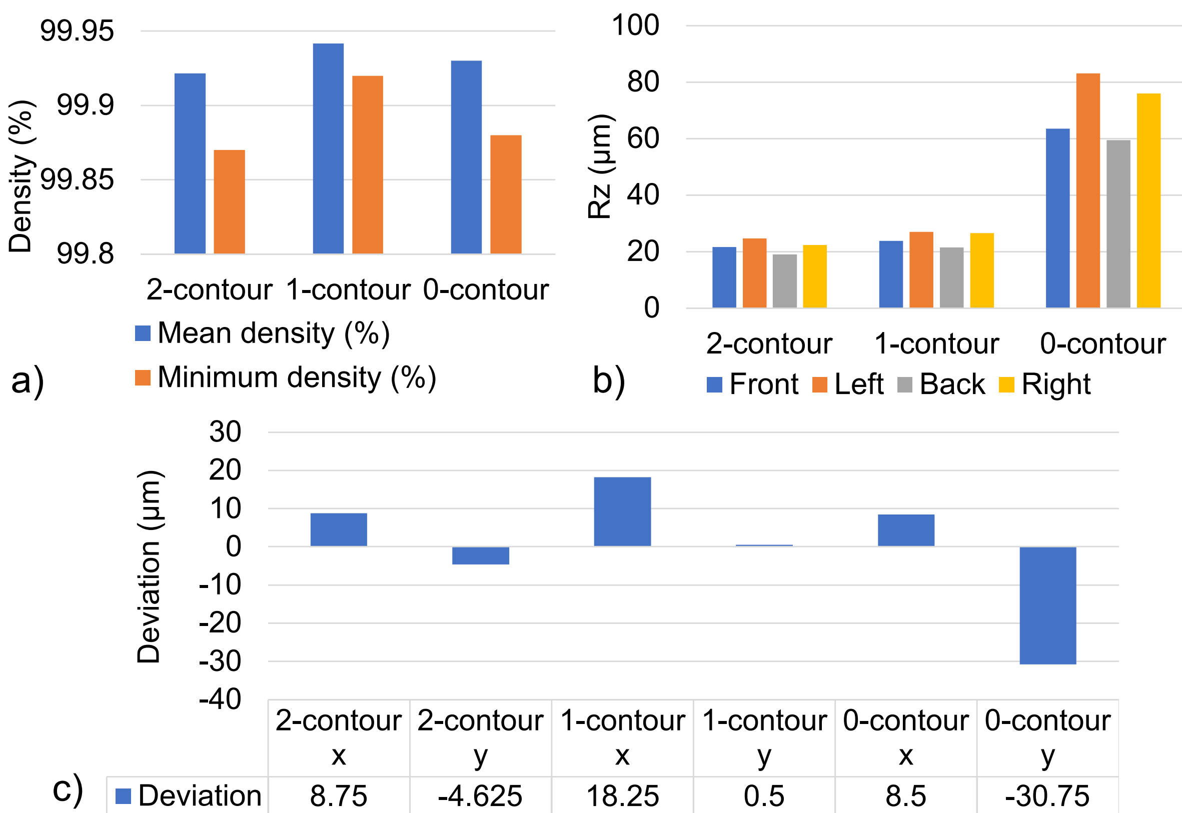


Figure A.15: a) Mean and minimum density before HIP (microscopy measurements), b) optical profilometry measurements of surface roughness (mean valley depth, $R_z$), c) size measurements of the difference from nominal (15 mm) between parallel faces.

## Appendix C. Surface profiles

Figure C.16 shows the minimum, mean, and maximum extents of the ray-casting measurements from the X-ray CT data for six complete specimens and their corresponding $S_v^{XCT}$ plots. Minor, regularly spaced variability in the minimum, mean, and maximum spaced at about 4 mm are likely imaging artifacts, and are eliminated by computing $S_v^{XCT}$.

## Appendix D. Combined S-N plots

The stress-life data points for all specimens tested are reproduced in Figure D.17, to allow more direct visual comparison between all four conditions. Note that confidence bands have not been shown here; see Figure 8 for the bands and their interpretation.

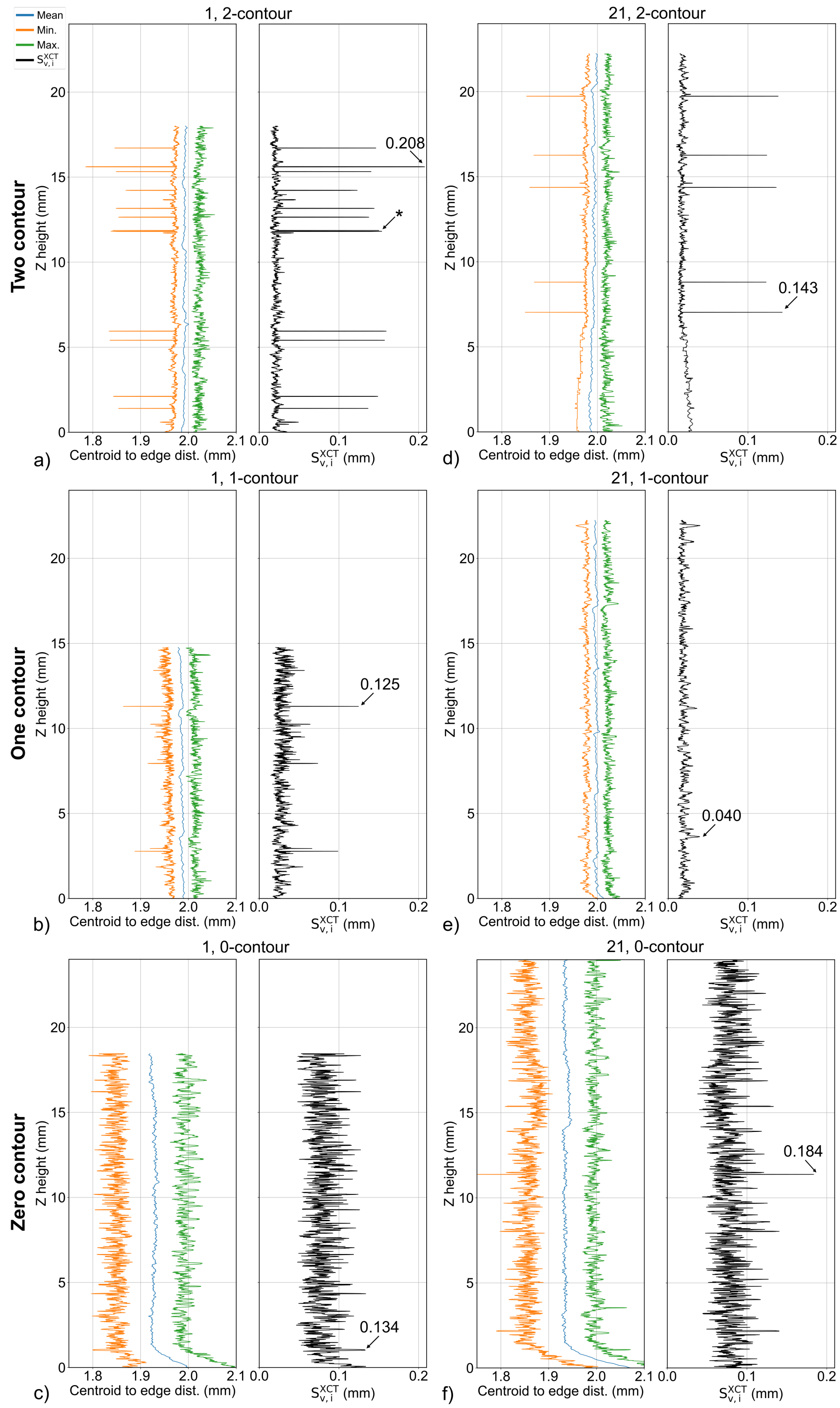


Figure C.16: Surface measurements derived from X-ray CT data for the shortest, mean, and maximum distance from the centroid to first non-metal pixel at each z-height for six specimens: a) location 1, 2-contour, b) location 1, 1-contour, c) location 1, 0-contour, d) location 21, 2-contour, e) location 21, 1-contour, e) location 21, 0-contour.

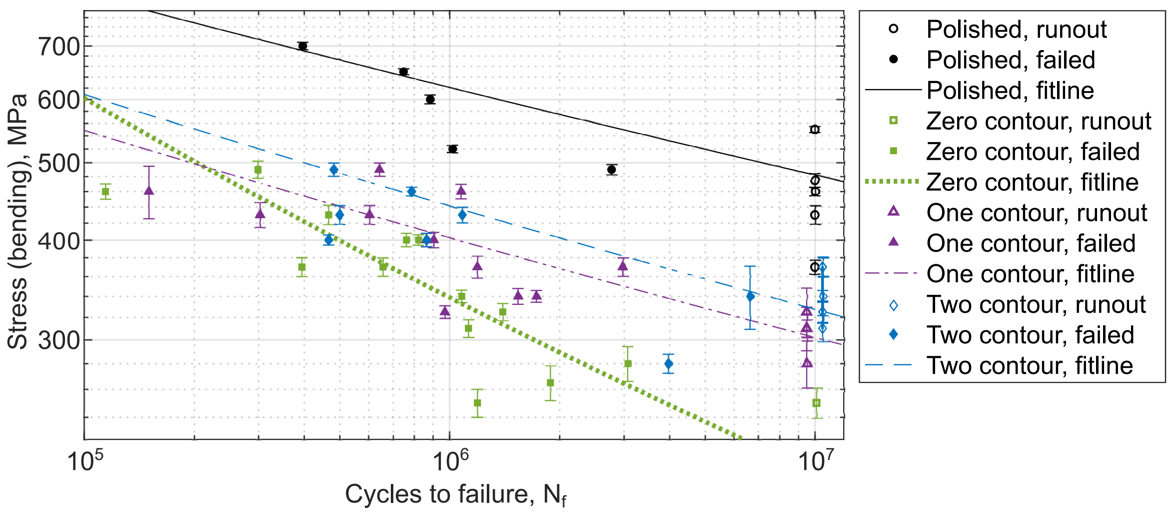


Figure D.17: Stress-life plots showing data points, fit line, and error bars as described in Section 2), combined into one axes, to directly compare all conditions.